Acta Materialia 216 (2021) 117146

Contents lists available at ScienceDirect

Acta Materialia

journal homepage: www.elsevier.com/locate/actamat

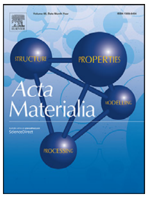

Full length article

Precipitation characteristics and distributions of subsurface hydrides in zirconium

Yu-Jie Jia[a], Irene J. Beyerlein[b,1], Wei-Zhong Han[a,*]

[a] Center for Advancing Materials Performance from the Nanoscale, State Key Laboratory for Mechanical Behavior of Materials, Xi'an Jiaotong University, Xi'an 710049, China
[b] Mechanical Engineering Department, Materials Department, University of California, Santa Barbara, CA 93106-5070, USA

ARTICLE INFO

Article history:
Received 4 April 2021
Revised 15 June 2021
Accepted 29 June 2021
Available online 4 July 2021

Keywords:
Zirconium
Hydride
Precipitation
Grain boundary
Basal plane

ABSTRACT

Hydride precipitates that develop in Zr after absorbing hydrogen can impart significant material hardening and embrittlement. Here, we use electrolytic hydrogen charging to synthesize Zr samples with different subsurface hydride aging times and transmission electron microscopy to understand the mechanisms underlying hydride precipitation and their distributions across the microstructure of pure Zr. Subsurface hydride formation involves volumetric swelling, causing the sample surface to produce bumps. Analysis of the morphologies and spatial distributions of these bumps can reveal several important characteristics of hydrides below. The analysis indicates that subsurface hydrides first form by isolated nucleation followed by coalescence. The shape of the hydride bump is found to be determined by the angle between the basal plane of the subsurface hydride and the sample surface. We reveal that, at room temperature, the hydride phase transition sequence follows γ-ZrH $\rightarrow\delta$-ZrH$_{1.66}$ $\rightarrow\varepsilon$-ZrH$_2$. The two main α-Zr/hydride orientation relationships are 1) $(0001)_\alpha||(11\bar{1})_\delta$ with $[2\bar{1}\bar{1}0]_\alpha||[011]_\delta$ or 2) $(0001)_\alpha||(001)_{\gamma}/_\delta$ with $[1\bar{2}10]_\alpha||[110]_{\gamma/\delta}$. Last, we show that the orientation of the basal plane plays a decisive role in the formation of both intragranular and intergranular subsurface hydrides. Statistical analysis of several hundred grain boundaries reveals that grain boundaries with c-axis misorientation of <15°, =55°-60° and >85° are preferential sites for subsurface hydride formation, while those with c-axis misorientations higher than 15° and one grain's basal plane nearly perpendicular to the grain boundary plane resist hydride precipitation. These findings can guide grain boundary engineering efforts for controlling hydrogen damage in Zr.

1. Introduction

Zirconium (Zr) and its alloys are widely used in nuclear reactors due to their excellent mechanical properties, high corrosion resistance and low neutron absorption cross-section [1-4]. In nuclear reactors, these alloys are exposed to hydrogen via two main sources: Zr-water corrosion reaction and water radiolysis [6]. Because of the extremely low solubility of hydrogen in Zr at ambient temperature [7-9], excessive hydride precipitation can readily occur. Hydrides are brittle and tend to form preferentially at stress concentrators. They can result in cracking [10-13] and additionally, induce blisters [5,14]. These phenomena all are causes of "hydride embrittlement", which is responsible for many reports of fracture incidents [5], limits the service life of Zr alloys, and results in reactor shutdown. In order to gain insight into ways to thwart their formation basic materials research has been devoted to understanding the precipitation [15-18], phase transformations, distributions in the microstructure [19-22], and deformation behavior of hydrides [23-27].

Hydrides have been observed to take on one of four different phases [1,28,29]: 1) trigonal ζ-Zr$_2$H, 2) face-centered tetragonal (FCT) (a<c) γ-ZrH, 3) face-centered cubic (FCC) δ-ZrH$_{1.66}$ and 4) FCT (a>c) ε-ZrH$_2$. The δ hydrides are frequently seen in Zr-alloy claddings and are the most detrimental phase [30,31]. The most common orientation relationship (OR) between α-Zr and the δ-hydride is $\{0001\}_\alpha||\{111\}_\delta$ and $<11\bar{2}0>_\alpha||<110>_\delta$ [19,21,32]. Many studies have been devoted to identifying the mechanisms underlying the growth of individual hydrides and hydride-hydride interactions [33-35]. Hydride precipitation involves a local volumetric expansion [36] and concomitant buildup of local stress. It is often accompanied by the emission of dislocations and dislocation loops [16,17]. Early hydride formation can affect char-

---

[*] Corresponding author.
E-mail address: wzhanxjtu@mail.xjtu.edu.cn (W.-Z. Han).

[1] Irene J. Beyerlein was an Editor of the journal during the review period of the article. To avoid a conflict of interest, Irene J. Beyerlein was blinded to the record and another editor processed this manuscript.

https://doi.org/10.1016/j.actamat.2021.117146

acteristics of subsequent hydride precipitation, such as inducing twinned hydrides [21,37-40] or stacked structures [35] or altering the hydride habit plane from the basal {0001} plane to the $\{10\bar{1}7\}$ plane or another plane [21,35,40]. Simulations have suggested that partial dislocation-mediated shear plays an important role in the transformation from α-Zr to a hydride [33,34]. It has been proposed that the twinned hydride results from the glide of partials with opposite Burgers vectors in the growing hydride front [21]. For the γ-ZrH hydride, while three variants of γ-ZrH have been reported to form along the three equivalent $<11\bar{2}0>$ directions, no fixed OR was observed between these hydrides and the α-Zr matrix [15]. Although these studies have provided useful results, more studies on the crystallographic characteristics of the different hydride variants and twinned hydrides are needed.

The transition and the stability between different hydride phases have also been discussed. It has been proposed that γ hydrides are the precursors for δ hydrides [41], and with increasing hydrogen, γ hydrides evolve into a mixture of γ and δ hydrides [42]. The γ hydrides have only been identified in samples after quenching [39], which would suggest that γ hydrides are an unstable phase [46,47]. It was observed that the δ hydrides tend to precipitate at relatively low cooling rates and anticipated that the δ hydrides can further develop into ε hydrides with more hydrogen absorption [43-45]. Clearly hydride stability still needs to be addressed. Further, many of these proposed mechanisms have not been confirmed by experimental observation.

Intergranular hydrides in Zr are of particularly concern because of their detrimental effects [48]. In general, hydrides prefer to nucleate at heterogeneous grain boundaries (GBs) over homogeneous sites inside grain [20]. Yet to date, contradictory reports exist among the many studies focused on the distributions and crystallographic characteristics of intergranular hydrides [19-22]. Theoretical calculations suggest that intergranular hydrides tend to nucleate at high-energy GBs, in which the basal planes of Zr are nearly parallel to the GB [19]. In contrast, some experiments have shown that the basal and prismatic tilt-GBs are both preferential sites for hydrides, while the angle between the GB surface trace and the basal plane of adjacent grains has no effect on hydride distribution [21]. Moreover, a closer look reveals that some GB hydrides are not exactly on the GB, and therefore, could not have originated there, but rather, it is likely they originated from the grain and grew to the GB [20-22]. Further, it has been reported that there are two to three different groups of intergranular hydrides with respect to their precipitation behavior, each warranting separate analysis [19-21]. Last, the relationship between different type of intergranular hydrides and the properties of the GBs on which they grow also needs to be clarified. A solution to this problem is to study and analyze large quantities of intergranular hydrides. However, analyzing statistically large datasets of intergranular hydrides and connecting these hydrides to their grain boundaries experimentally within the bulk of the sample still remain a challenge.

In this work, we study hydride precipitation using subsurface hydrides as a model case. Subsurface hydrides are easy to fabricate, track and analyze, facilitating characterization of the precipitation, morphology evolution, and spatial distribution of intragranular and intergranular hydrides under stress-free conditions. A similar method was also used in Ti [32], U [49] , Pd and Gd thin films [50,51] to study the behavior of hydride precipitation. Here, we used electron backscatter diffraction (EBSD), sample lift-out techniques, and a suite of microstructural characterization methods to study subsurface hydride in grains and along GBs. The findings made in the present study on subsurface hydrides can help to develop understanding of hydrides within bulk samples.

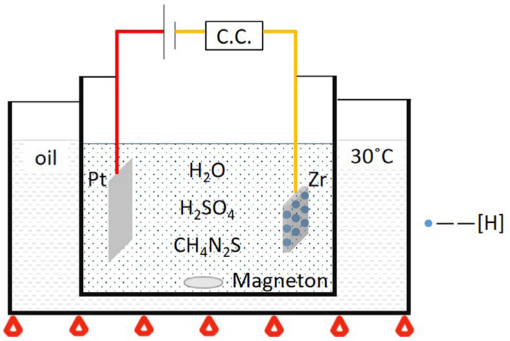

Fig. 1. Schematic showing the setup for electrolytic hydrogen charging.

2. Experimental methods

2.1. Hydrogen charging

High-purity Zr with an average grain size of ~85 μm was used in this study. Before charging, the samples were ground and etched in a solution of HF: HNO_3: H_2O=3:40:57 for about one minute in order to remove the surface oxide layer. After this pickling step, the polished surface of the samples was used for hydrogen charging, while all other faces were sealed by a hot-melt adhesive to limit hydrogen absorption. Hydrogen charging was conducted electrochemically in a solution of 0.5 mol/L sulfuric acid using a current density of 0.2 A/cm^2 at 30°C. Next, a 2 g/L thiourea was added to hinder hydrogen recombination and gas generation [52]. Fig. 1 shows the setup for hydrogen electrolytic charging. An oil bath was placed underneath to maintain thermal stability and a magneton was used to accelerate heat conduction and homogenize the solution. Charging times of 10 min, 30 min, 1 h, 3 h, 6 h, 12 h, 24 h and 48 h were selected in order to achieve different densities and ages of the subsurface hydride.

2.2. Microstructure characterization

After charging, the microstructure of samples was characterized by X-ray diffraction (XRD), scanning electron microscope (SEM, SU6600), and transmission electron microscope (TEM, JEOL 2100F). XRD was employed to identify the phase structure of subsurface hydrides and SEM was used to study the subsurface hydride-induced bumps. TEM analysis was carried out to examine the microstructure of the subsurface hydride. The TEM samples were prepared using a sample lifting technique inside a focus ion beam (FEI Helios Nanolab600). Platinum (Pt) was deposited on the top of the hydride bumps to avoid ion-beam damage. TEM samples with dimensions of 15 μm × 10 μm × 2 μm were cut. These TEM foils were further thinned down to about 100 nm and polished with a gentle Ga$^+$ beam (5 kV voltage and 48 pA beam current).

EBSD was utilized to determine the orientation of the grains and the misorientations and characteristics of the GBs. EBSD analysis was performed inside a focused ion beam, with an Oxford HKL Nordlys EBSD detector, with a voltage of 20 kV and probe current of 2.7 nA. The size of each scan was 260 μm × 226 μm at a step size of 2 μm. The size, number density and aspect ratio of each hydride bump on samples with different charging times were measured using Image-pro software. The area fraction of the hydride bumps was determined by measuring the area of the Zr first and subtracting it from the entire scanned area. The GB characteristics were determined from the orientation (in Euler angles) of the adjacent grains. We also calculated the GB c-axis misorientation, defined as the minimum angle between the [0001] directions of the two adjoining grains, since it has been identified as influential in the behavior of intergranular hydrides [21]. To study the effect of

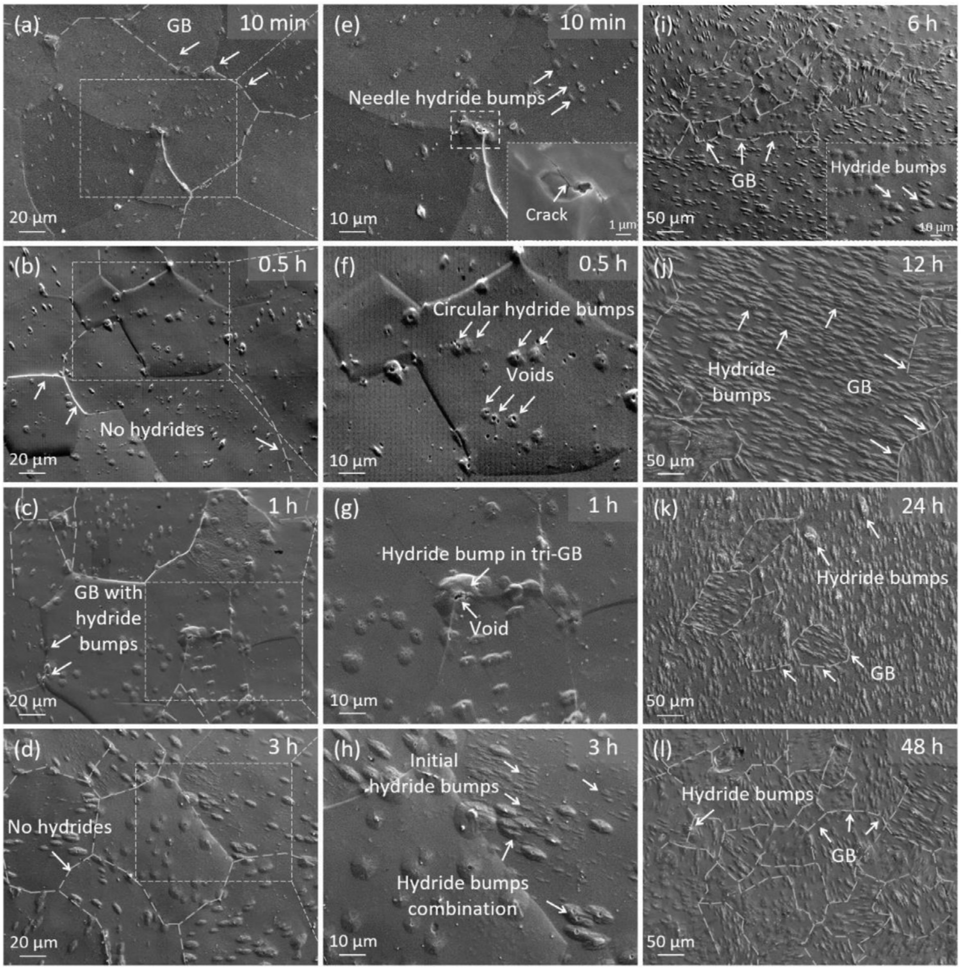

Fig. 2. Surface hydride bumps in Zr after electrolytic hydrogen charging at different times (a) and (e) 10 min, (b) and (f) 0.5 h, (c) and (g) 1 h, (d) and (h) 3 h, (i) 6 h, (j) 12 h, (k) 24 h and (l) 48 h. (e), (f), (g) and (h) Enlarged images for the regions shown by white squares in (a), (b), (c) and (d), respectively.

the GB plane orientation on the intergranular hydrides, we considered only those hydrides lying on the narrowest (width) GBs. GB planes of narrow GBs tend to be perpendicular to the sample surface, which have edge on position [53]. Statistical analysis of the characteristics of the GBs and hydrides included hundreds of GBs.

3. Results

3.1. Morphology of subsurface hydride bumps

Fig. 2 shows the number, distribution, and morphologies of the hydride bumps after different charging times. The number of bumps increases with charging time. The formation of surface bumps is a direct indication of the precipitation of subsurface hydrides. All bumps are solid and a consequence of the volume expansion associated with subsurface hydride formation [36]. Voids and surface cracks resulting from this expansion can be seen at the top of the bumps, in Fig. 2(e) and (f). These bumps are different from hydrogen blistering, which is caused by temperature gradients induced by high levels of hydrogen concentration [5]. The spatial distribution of these hydride bumps are suggestive of either their nucleation (Fig. 2(a)), growth (Fig. 2(b) and (c)) or combination of the two (Fig. 2 (i) to (l)). In this figure, the white dash lines indicate GBs. First, most hydride bumps are located inside the grains (Fig. 2), similar to hydrides in coarse-grained Zr [21,54]. Second, only a small fraction of bumps lies in the GBs (Fig. 2(g) and (h)). Most GBs are free of hydrides (Fig. 2(b) and (d)). Third, more than 58% of the triple junctions have hydride bumps, implying that hydride bumps prefer to form and coarsen at the triple junction of GBs (Fig. 2(g)). Fourth, the long-axis orientation of hydride bumps in the same grain are similar but vary from grain to grain, as seen in Fig. 2(i) to (l). Last, we observe in shown in Fig. 2(e) and (f) that the bump morphology can be categorized as either circular-like or needle-like.

Understanding the stages in hydride formation can be attained by studying the evolution in their morphologies with increasing charging time. Fig. 3 shows the continuous rise in the area fraction of hydride bumps as charging time increases from 10 min to 12 h. For longer charging times (up to 48h), their area fraction saturates (Fig. 3(a)). The final area fraction reaches nearly 80%. Fig. 3(b) shows the evolution of hydride bump size and number density. Bump size increases from a few μm to around 20 μm at 12 h, then slightly decreases from 12 h to 48 h. The number density of bumps gradually increases from 10 min to 6 h, indicating that nucleation and growth of subsurface hydride dominate in the earlier stages of charging. After 6 h, the bumps coalesce and coarsen, causing their number density to decrease. Fig. 3(c) shows the variation in the aspect ratios of the needle-like and circular-shape hydride bumps with charging time. For all charged samples, the needle-like bumps maintain an aspect ratio of slightly larger than 2, while the circular-like bumps maintain an aspect ratio of around 1. This analysis of the changes in hydride bump morphology with charging time suggests that hydride bump formation can be divided into two consecutive stages: isolated nucleation (10 min to 6 h) and coalescence (6 h to 48 h). The transition to the second

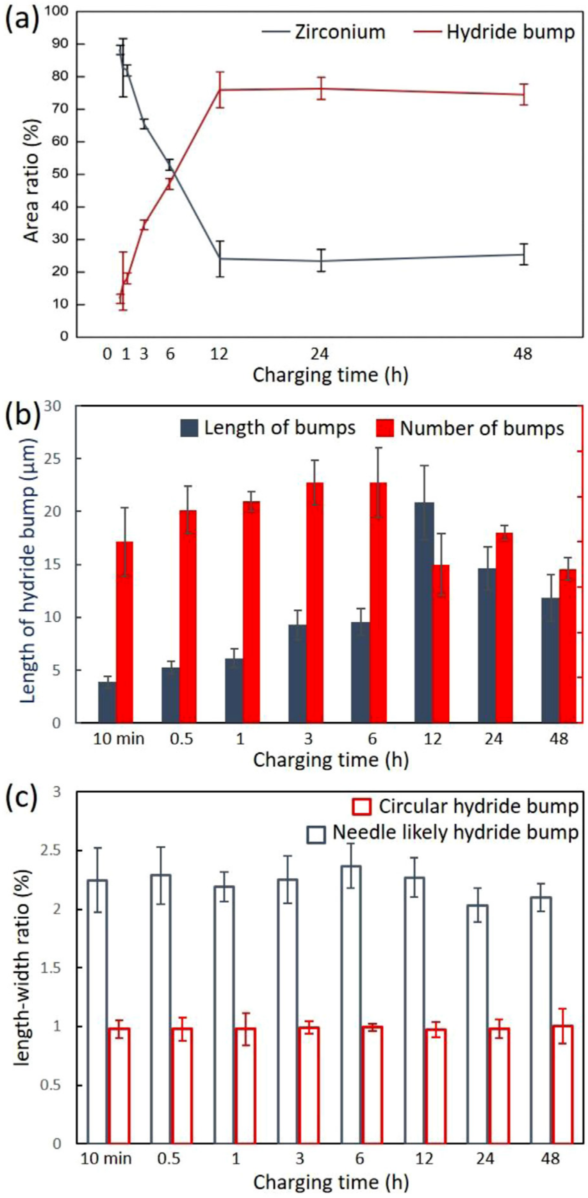

Fig. 3. (a) Variation in the area fraction of hydride bumps/Zr matrix with increasing charging time. The data are based on two 500 × EBSD images (260 μm × 226 μm). (b) Statistical analysis of the length and number density of hydride bumps for different charging times. The length and number density of hydride bumps in each charging time are obtained based on three 1000 × SEM images (125 μm × 90 μm) and averaged. (c) The aspect ratio of hydride bumps with different charging times.

stage begins once the growing hydride bumps start to coalesce, as marked in Fig. 2(j).

Hydride bump morphologies are expected to depend on the underlying lattice orientation of the grain [32]. To identify orientation effects, we use EBSD to relate hydride bump morphology with the orientation of the underlying grain (Fig. 4). Because the most common habit plane of hydrides is nearly {0001} [21,35], when the basal plane of Zr matrix is nearly parallel to the sample surface, the hydride bumps grow equally in the three <11$\bar{2}$0>-type directions [36], forming a circular-like shape (Fig. 4(a) and (b)). Conversely, when the basal plane of the grains makes a large angle with the sample surface, the long axis of the hydride bump becomes roughly parallel to the {0001} plane of the grains, forming a needle-like bump (Fig. 4(b) and (c)). For neighboring grains close in orientation, hydride bumps span both grains, as shown in Fig. 4(b). Evidently, the interacting angle between the basal plane and the sample surface influences the shape of the hydride, whether circular-like or needle-like.

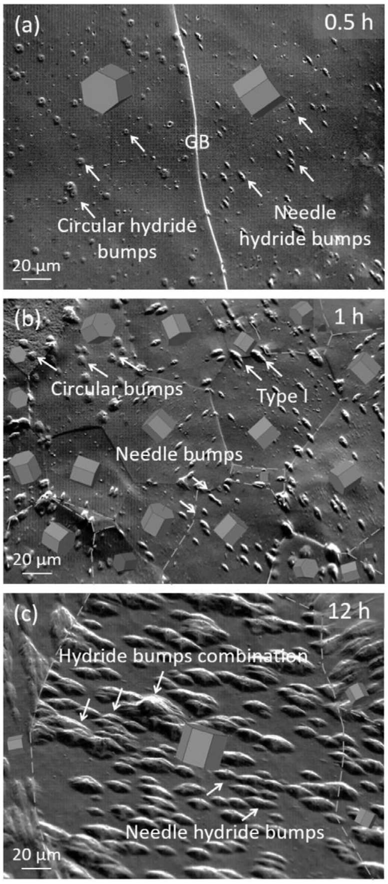

Fig. 4. Orientation relationship (OR) between hydride bumps and Zr grains determined by EBSD. (a) 0.5 h, (b)1 h and (c) 12 h. These HCP unit cells mark the orientations of Zr grains.

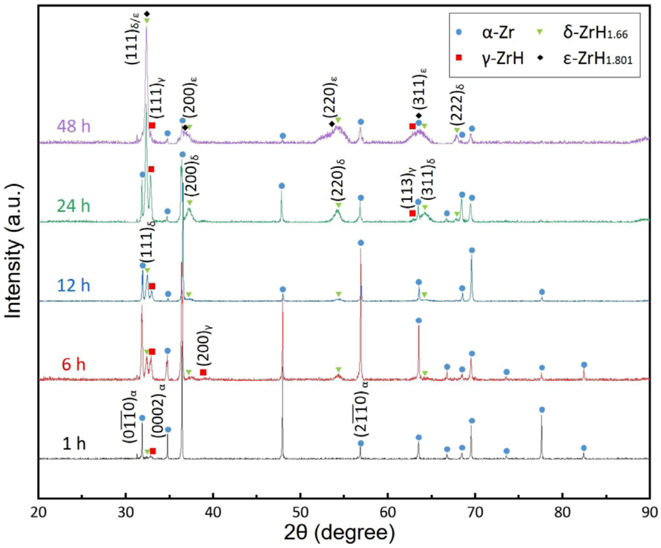

Fig. 5. XRD patterns of pure Zr samples with different charging times. Three types of hydrides are identified in these samples.

3.2. Phase structure and microstructures of subsurface hydrides

XRD was used to identify the structure of the hydride. Fig. 5 presents the diffraction data for samples with different charging times. For the sample with the 1 h charging time, besides the sig-

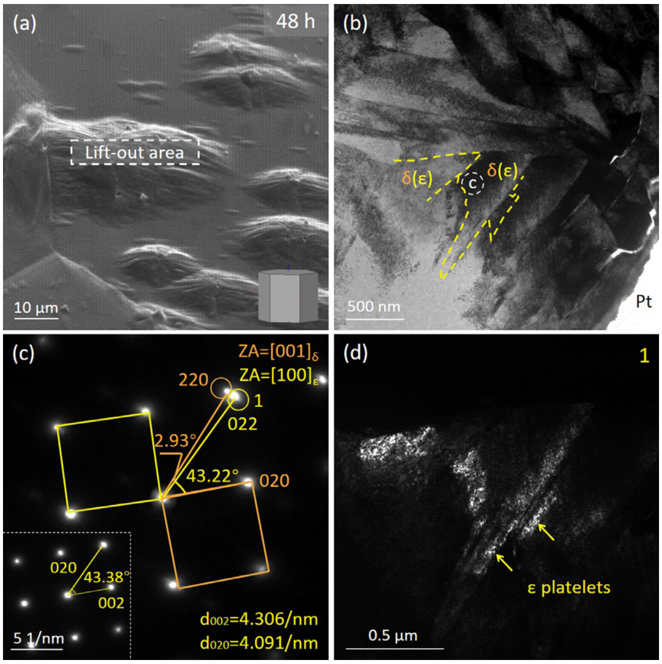

Fig. 6. Typical TEM images of subsurface hydrides viewed along the $[0001]_\alpha$ zone axes after hydriding for 48 h. (a) A combined hydride bump is selected as the lift-out area. (b) Underlying microstructures of the bump. (c) Diffraction pattern showing the OR between the δ and ε hydrides. The small image in the left is the diffraction pattern of ε hydrides and obtained by using the smallest objective aperture to observe the white dash circle area in (b). (d) Dark-field images of the ε hydrides platelets.

nal associated with the Zr matrix, (111) peaks associated with the γ-ZrH and δ-ZrH$_{1.66}$ hydrides appear. The (111) peak of γ-ZrH is much greater than that of δ-ZrH$_{1.66}$, indicating that the precipitation of γ-ZrH is dominant in the earlier stages of hydrogen charging [30]. When charging for 6 h, the (111) peaks of γ-ZrH and δ-ZrH$_{1.66}$ reach a similar level. In addition to the (111) peak, other diffraction peaks associated with these hydrides start to increase and their volume fractions grow (Fig. 3(a)). The heights of the (111) peak of δ-ZrH$_{1.66}$ in samples charged for 12 h and 24 h are much higher than that for γ-ZrH. This change indicates that the γ-ZrH is gradually transforming into δ-ZrH$_{1.66}$. In the samples charged for 48 h, the diffraction peak of γ-ZrH almost disappears, while the δ-ZrH$_{1.66}$ is still the dominant phase. Additionally, the diffraction peaks of ε-ZrH$_2$ start to appear, as shown by the black spots in Fig. 5. The transition can be further confirmed by the 48h sample lift-out results shown in Fig. 6. The diffraction pattern in Fig. 6(c) indicates the formation of ε-ZrH$_2$ hydrides. The newly formed ε hydrides are embedded in the δ hydrides and exhibit a stripe-like structure. The habit plane of the ε hydride is within 3°of the $\{011\}_\delta$ plane [43,45]. Hence the transition from δ-ZrH$_{1.66}$ to ε-ZrH$_2$ takes place when the charging times are less than 48 h. The volume of ε-ZrH$_2$ unit cell (93.88 Å^3) is 7.8% smaller than that of δ-ZrH$_{1.66}$ (101.85 Å^3) [29]. Thus, the reduction in length and number density of hydrides with 48 h of charging seen in Fig. 3 is likely associated with the δ-to-ε hydride transition. The XRD and TEM results show a phase transition sequence of γ-ZrH → δ-ZrH$_{1.66}$ → ε-ZrH$_2$ under continuous hydrogen charging.

To further investigate the microstructures of subsurface hydride and their relationship with surface hydride bumps, thin foils were cut from the top of subsurface hydrides and examined, as shown in Figs. 7 to 9. The 1 h sample was chosen for thin-foil cutting, since several bumps from the same thin foil could be examined. Before lift-out, EBSD was used to identify proper viewing orientation. We used in Figs. 7 (a) and 8(a) the $<11\bar{2}0>_\alpha$ and $<0001>_\alpha$ zone axes as viewing directions, which are the long and transverse directions of the bumps, respectively. The microstructures of the three bumps shown in Fig. 7(a) are highlighted in Fig. 7(b) to (e), respectively. According to the selected area electron diffraction (SAED) pattern in Fig. 7(f), these bumps contain parallel δ subsurface hydride platelets. The OR between the δ hydrides and α-Zr is $(0001)_\alpha||(11\bar{1})_\delta$ and $[2\bar{1}\bar{1}0]_\alpha||[011]_\delta$, and the habit plane of the hydrides is {0001}. Figs. 7(g) to (i) show dark-field images taken by selecting the diffraction spots in Fig. 7(f). These parallel hydride platelets have a twin OR, with a $(111)_\delta$ twinning plane (Fig. 7(i)). Besides the major δ hydrides formed near the sample surface, there are many smaller lenticular-shaped hydrides beneath them, as shown in Fig. 7(g) and (i).

Figs. 8 and 9 show some of the key characteristics of the hydrides that can be captured when viewing along the [0001] zone axis. Fig. 8(a) shows four hydride bumps. The needle-shaped hydrides shown are γ-ZrH. Three variants of the γ-ZrH hydride intersect at angles of nearly 60° or 120°. According to the SAED pattern in Fig. 8(e), their growth direction lies along $<\bar{1}2\bar{1}0>_\alpha$. The OR between γ-ZrH and α-Zr is $(0001)_\alpha||(001)_\gamma$ and $[1\bar{2}10]_\alpha||[110]_\gamma$. Underneath the four hydrides in Fig. 8(a) are two types of δ-ZrH$_{1.66}$, labeled as δ_1 and δ_2 in Fig. 9(a)). Because of the similar d-spacing between the γ (FCT) and δ (FCC) hydrides under the [001] zone axis, diffraction along the $[\bar{1}14]$ and [013] zone axes were both collected in order to confirm their identity (Figs. 8(f) and 9(d)). The OR between the needle-like δ_2 hydrides and α-Zr matrix is $(0001)_\alpha||(001)_\delta$ and $[1\bar{2}10]_\alpha||[110]_\delta$, which is similar to that of the γ_2 hydrides in Fig. 8. The habit plane of the δ_2 hydrides is also {0001}. This observation provides direct evidence for the transformation of γ_2 hydrides into δ_2 hydrides with increasing hydrogen loading. Additionally, further evidence of the γ-to-δ transformation is provided by the (110) spot in Fig. 9(b) and the complete disappearance of the (110) spot in Fig. 9(c). For the FCC δ hydrides, the {110} spots are extinction, but not for FCT γ hydrides. Therefore, for the region labeled c in Fig. 9(a), the hydride is near the surface and sufficient hydrogen supports the full phase transition. In contrast, for the region designated by b & d in Fig. 9(a), the hydride is slightly far from the sample surface, and the appearance of the (110) spot indicates a mixture of γ and δ hydrides, indicating a partial γ-to-δ hydride phase transformation. In addition to the δ_2 hydrides, δ_1 hydrides had an OR of $(0001)_\alpha||(11\bar{1})_\delta$ and $[2\bar{1}\bar{1}0]_\alpha||[011]_\delta$, as shown in Fig. 9(c). Under the viewing direction of $[0001]_\alpha$, the morphology of the δ_1 hydride is found to be plate-like.

4. Discussion

4.1. Crystallographic characteristics of subsurface hydrides

Analysis of the crystallographic characteristics reveals that each hydride has its own preferential orientation relationship with α-Zr. For reference, Fig. 10 shows the crystal models and corresponding crystallographic OR for both the γ and δ hydrides. For the δ-ZrH$_{1.66}$ hydrides, the crystal structure is classified as $Fm3\bar{m}$, and for α-Zr, P63/mmc. For both the matrix and twinned δ hydrides, the OR is given by $(0001)_\alpha||(11\bar{1})_\delta$ and $[2\bar{1}\bar{1}0]_\alpha||[011]_\delta$. Different from the $\{10\bar{1}3\}$ interface plane of the B-type hydride in Ti [32], the interface between hydride and Zr for the first OR is nearly {0001}, which is also the habit plane of the hydride. This leads to a different anisotropic misfit and contributes to the formation of multiple hydride platelet variants. In Zr, however, only two variants exist. The crystallographic OR of the twinned δ hydrides is given by rotating the matrix δ hydride phase along the <111> axis by 60°. In an earlier report [39], the formation of the twin structure was thought to occur via non-equilibrium precipitation. However, more recently, it was proposed that the precipitation of twin hydrides

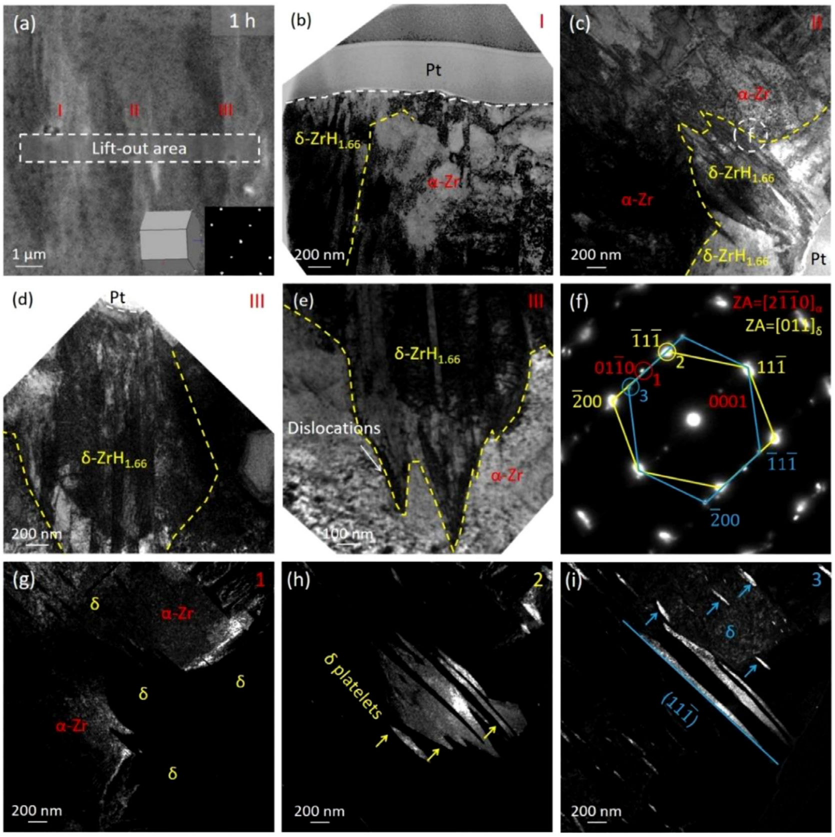

Fig. 7. Typical TEM images of subsurface hydrides formed after electrolytic hydrogen charging for 1 h. (a) The SEM image displays the top view of three hydride bumps. (b), (c), (d) and (e) TEM images correspond to the three hydride bumps in (a). These images were taken under the $[2\bar{1}\bar{1}0]_\alpha$ zone axes. (f) Selected area electron diffraction of the region shown by a white dash circle in (c). (g) to (i) Dark-field images displaying the α-Zr matrix and twinned hydrides using diffraction spots shown in (f).

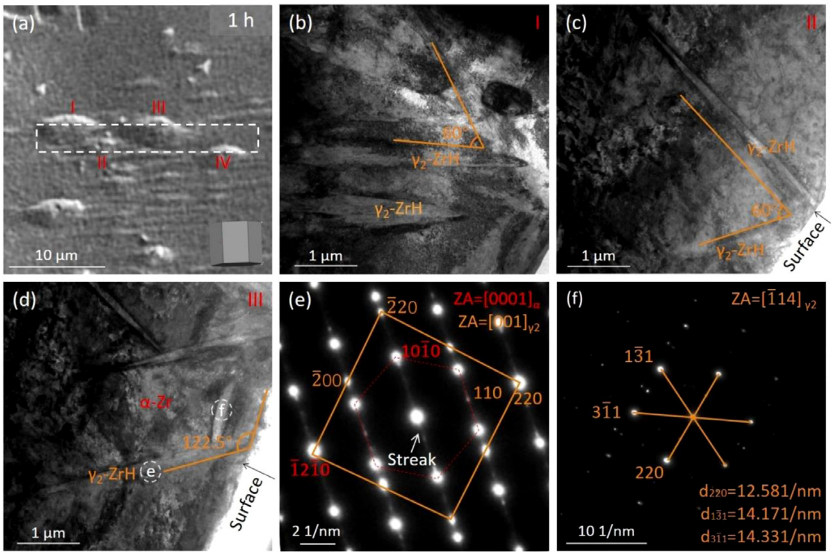

Fig. 8. Typical TEM image of subsurface hydrides viewed along the $[0001]_\alpha$ zone axes. (a) Four hydride bumps were examined. (b) to (d) highlight the microstructures of γ hydrides underneath hydride bumps labeled in (a). (e) and (f) are the selected area electron diffraction pattern for the region shown in (d). (e) The OR between γ hydrides and Zr matrix. (f) Diffraction pattern of γ under the $[\bar{1}14]$ zone axes.

is mediated by the glide of Shockley partial dislocations with opposite Burgers vectors [21]. Here, this proposition is corroborated by the results in Fig. 7(h) and (i), which show that the matrix and twin hydrides are alternatively stacked. The formation of twin hydride structures, therefore, is a dislocation-mediated mechanism to relieve local stress concentrations from hydride precipitation.

For the γ hydrides, the OR is $(0001)_\alpha||(001)_{\gamma/\delta}$ and $[1\bar{2}10]_\alpha||[110]_{\gamma/\delta}$. Hydrides with this OR only can be seen under the $[0001]_\alpha$ zone axis (Figs. 8 and 9). This OR also applies to the transition from a γ to δ hydride. Fig. 10(b) displays the spatial distribution of the subsurface hydrides with this OR. Three equivalents $<1\bar{1}00>$ directions lie in the $(0001)_\alpha$ plane, all of which are preferred growth directions for both the γ and δ hydrides with second type of OR, which is different from early report [15]. Accordingly, three needle-shape hydride variants can be observed (Figs. 8 and 9). The orientations of the three hydride variants differ

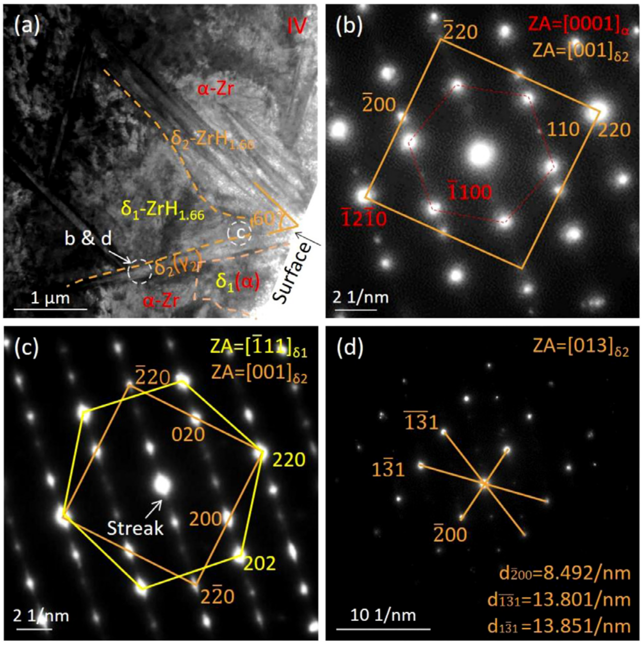

Fig. 9. (a) Microstructure underneath the hydride bump IV in Fig. 8(a). (b) Diffraction pattern showing the OR between the α-Zr and γ_2/δ_2 hydride. (c) Diffraction pattern displaying the OR between δ_1 and δ_2 hydrides. (d) Diffraction pattern of δ_2 hydride with a zone axes of [013].

by a 60° rotation around the $[001]_\delta$ zone axes. The appearance of streaks in the diffraction pattern in Figs. 8(e) and 9(c) suggests the formation of profuse stacking faults during hydride precipitation [55]. This observation supports the proposal that the formation of stacking faults may be achieved by the glide of $\frac{a}{3}<1\bar{1}00>$ partial dislocations in Zr [21].

The first OR seen with the δ hydrides observed in Fig. 7 is a common one [19,21] and, as expected, joins the closest-packed planes of the phases. For the second OR with the γ hydrides in Fig. 8, two lattice spacings are possible: $d_{(111)} = 2.7196$ Å and $d_{(001)} = 4.969$ Å. Compared to the former, the latter spacing is much closer to the $d_{0001} = 5.147$ Å of α-Zr, leading to a smaller dilatational strain, and likely preference for the $d_{(001)}$ than $d_{(111)}$ [56,57]. Nonetheless, hydrides with both ORs can be produced during the earlier stage of hydride precipitation and, with both, comes significant volume expansion [36], i.e., 12.3% for γ hydrides and 17.2% for δ hydrides, the cause for the hydride bumps (Figs. 2 and 10). The high-density of dislocations observed in the front of the hydride tip (Fig. 7(e)) [17,18], as well as the formation of a stacking structure seen in Figs. 7 and 9 are mechanisms that could relieve the dilatational strain associated with the volumetric expansion [35].

4.2. Stability and phase transformation of subsurface hydrides

In this study, three types of hydrides were observed: γ-ZrH, δ-ZrH$_{1.66}$ and ε-ZrH$_2$ hydrides. The present XRD and TEM analyses suggest that they are related by the following precipitation sequence of $\gamma\text{-ZrH} \rightarrow \delta\text{-ZrH}_{1.66} \rightarrow \varepsilon\text{-ZrH}_2$. With this, the question arises as to whether γ hydrides are stable under ambient conditions. Over the years, many studies have confirmed that under stress-free conditions and slow cooling rates, δ hydrides can form easily, whereas γ hydrides, however, can only form when quenched [39,46,47]. The XRD data in Fig. 5 provide clear evidence for the precipitation of γ hydrides in the early stages of hydrogen charging. With further increases in hydrogen loading, the same data suggest δ hydrides or ε hydrides become preferred (Fig. 5) [58]. For hydrides with the second OR type, i.e., $(0001)_\alpha||(001)_{\gamma/\delta}$ and $[1\bar{2}10]_\alpha||[110]_{\gamma/\delta}$), γ hydride formation is preferred over δ formation [40]. Because the γ hydride has an FCT (c>a) crystal structure, $d_{(001)}$ is smaller and much closer to the d-spacing of $(0001)_\alpha$ of α-Zr, than the $d_{(111)}$ of δ hydride [56,57], which can reduce the dilatational strain associated with the phase transformation. The stability of the γ hydride at room temperature can be further understood based on thermodynamic data. Density functional theory calculations report negative formation enthalpies of both γ and δ under ambient conditions [29]. The enthalpy of the γ hydrides is slightly lower than that of the δ hydrides over a large temperature range from 0 K to 700 K [59]. Therefore, the γ hydride is expected to be more stable than the δ hydride at ambient temperature.

Heating is the main driving force for the γ-to-δ transformation [46,47,60], bringing into question whether the γ-to-δ transformation is possible at room temperature. In this work, we find direct evidence for room temperature γ-to-δ hydride transformation based on both XRD data and TEM observations (Figs. 5 and 9). This result contradicts many earlier reports that suggest that the γ-to-δ transition occurs at high temperature. Under aging at above 200°C, it has been reported that the volume fraction of the γ hydrides decreases and that of the δ hydrides increases [46,47]. A γ hydride layer was seen to form at the tip of δ hydrides in Zircaloy-2 after cooling from high temperature [41]. The continu-

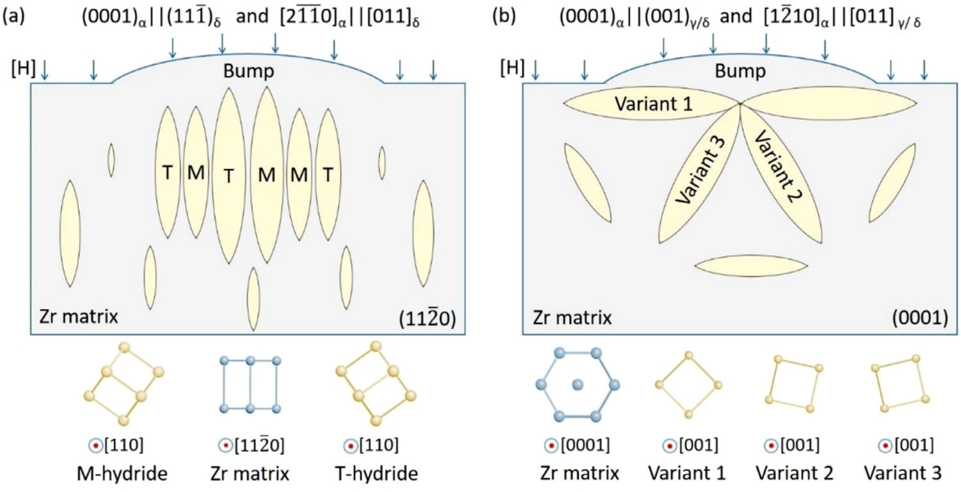

Fig. 10. Schematic showing microstructures of subsurface hydrides with two different ORs and the volume expansion induced bumps. All the yellow needle-like variants represent subsurface hydrides. (a) Subsurface hydrides with OR of $(0001)_\alpha||(11\bar{1})_\delta$. (b) Subsurface hydrides with OR of $(0001)_\alpha||(001)_{\gamma/\delta}$.

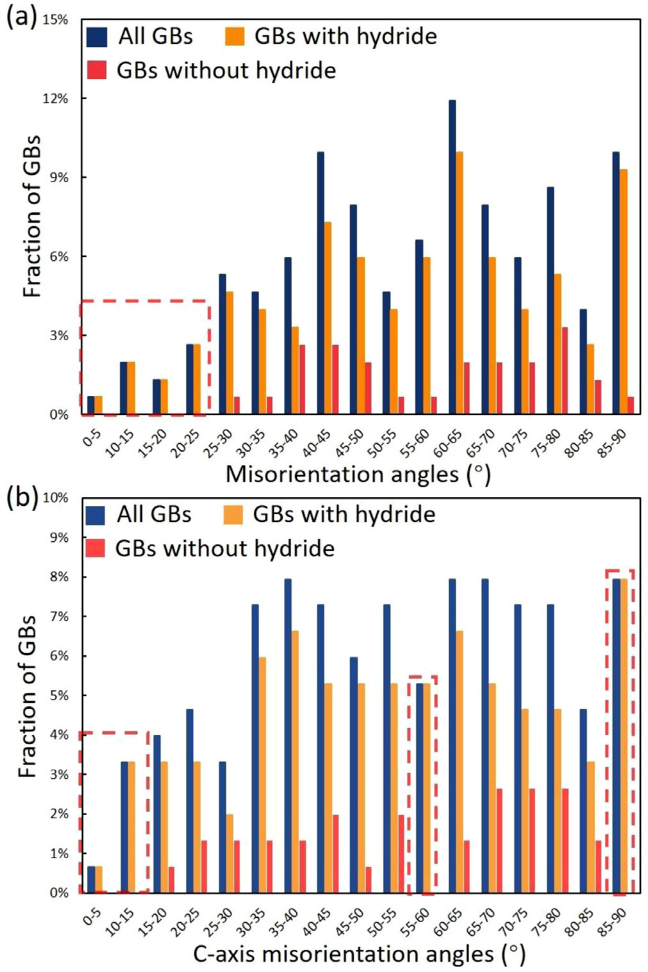

Fig. 11. Statistics showing the relationship between the GB characteristics and hydride precipitation. (a) GB misorientation vs. hydride. (b) GB c-axis misorientation vs. hydride. The statistical data set contains 151 GBs based on samples charging for 10 min, 0.5 h and 1h.

ous charging used in the present experiment could have provided sufficiently large amounts of hydrogen to promote the phase transformation even at room temperature. Another likely driving force the room-temperature phase transformation seen here is related to the stacking structures around the γ_2 hydrides (i.e., the streaks in Fig. 8(e)). After δ_2 hydride formation in area b in Fig. 9(a), the streaks along the (220) plane in the diffraction pattern disappear, indicating that stacking structures are consumed during phase transition, as shown in Fig. 9(b).

4.3. Effect of grain boundary characteristics on intergranular hydride

Experimental studies have reported that GB characteristics can influence hydride precipitation [19-22], opening up the possibility that GB engineering can be used to control it. The hydride bumps examined here can provide a suitable model system to explore the connection between GB characteristics and intergranular hydride growth. Surface bump formation results from the local volumetric expansion associated with hydride precipitation and, therefore, can be linked to where hydrides formed subsurface.

According to the statistical analysis shown in Fig. 11, hydrides prefer to nucleate on GBs with misorientations that are less than 25° or with c-axis misorientations less than 15°, near 60° or near 90°. Similarly, a recent experiment has shown that intergranular hydrides tend to form on GBs with c-axis misorientations of less than 40° or higher than 80° [21]. Further analysis in Fig. 11(a) and (b), finds that compared to the complete GB misorientation, the c-axis misorientation is the more appropriate parameter affecting hydride formation at GBs. Fig. 11(b) reveals that hydrides prefer (with 100% hydride formation) to nucleate on GBs with the basal plane in the neighboring grains nearly parallel [19], perpendicular [21] or lying at an interacting angle of about 60°, which likely can be explained either by the low energy of symmetric tilt grain boundaries near this angle [61] or by the $\{10\bar{1}1\}$ secondary habit plane of hydrides [62]. To limit intergranular hydrides, the volume fraction of these types of GBs should be reduced.

Toward designing for limited hydride formation, GBs without hydrides are also plotted in Fig. 11 (red columns). We see that more than 55.5% of GBs with misorientations in the range of 25° to 90° have hydrides, which indicates that some GBs in this range resist hydride formation. More than 72% of the other GBs have partial hydride precipitation (Fig. 10(b)). A closer analysis identifies that those GBs with misorientations or c-axis misorientations in the range of 30° to 55° and 65° to 85° are resistant to hydride precipitation.

In this study, three intergranular hydride bump morphologies were identified. Type I bumps span across a GB, appearing to grow on both sides of the GB, as shown in Fig. 12(a). Type II bumps, in contrast, involve two different growth orientations and appear to intersect at the GB. Therefore, type II hydride bumps contain an interface, as shown in Fig. 12(b). Both type I and type II hydrides likely nucleated at GBs and grew into the adjoining grains. Type III bumps grow only on one side of the GB or lie solely within the GB, as shown in Fig. 12(c).

Fig. 12(d) and (e) shows the results from a statistical analysis of the main characteristics of these three intergranular hydride morphologies. A majority of the type I hydride bumps form on GBs with c-axis misorientations less than 40°, as shown in Fig. 12(d). For smaller c-axis misorientations, the misfit strains at the boundary are sufficiently small that the subsurface hydride can still preserve a similar growth orientation [21]. This is perhaps why hydrides are much larger than the grain size and maintain a similar orientation in strongly textured Zr alloys [63]. In contrast, all type II hydride bumps are connected to GBs with c-axis misorientations larger than 40°. Growth of these type II hydrides tend to follow their parent grain orientation once the c-axis misorientation exceeds 40°, as shown in Fig. 12(b). Type III hydride bumps only occupy a small fraction of the hydrides observed and exhibit a strong preference for GBs that include the basal plane of a neighboring grain interacting at an angle of more than 75° with the GB plane, as shown in Fig. 12(e).

Additionally, the characteristics of GBs without hydride formation are also plotted versus the angle between the basal plane and GB plane in Fig. 12(f). Interestingly these hydride-free GBs also have one grain with the basal plane nearly perpendicular to the GB plane. These GBs are similar to the GBs associated with type III hydride bumps that only form on one side of the GB or just intersect the GB, while not being nucleated from it. Furthermore, the c-axis misorientations of the GBs in Fig. 12(e) and (f) are all higher than 15°. Based on these observations, we conclude that the GBs with at least one neighbor grain c-axis nearly perpendicular to the normal direction of the GB plane and with c-axis misorientations higher than 15° are resistant to hydride precipitation. A possible explanation for this phenomenon is that the orientation of the adjoining grains hinders subsurface hydride growth across the common GB [19,22].

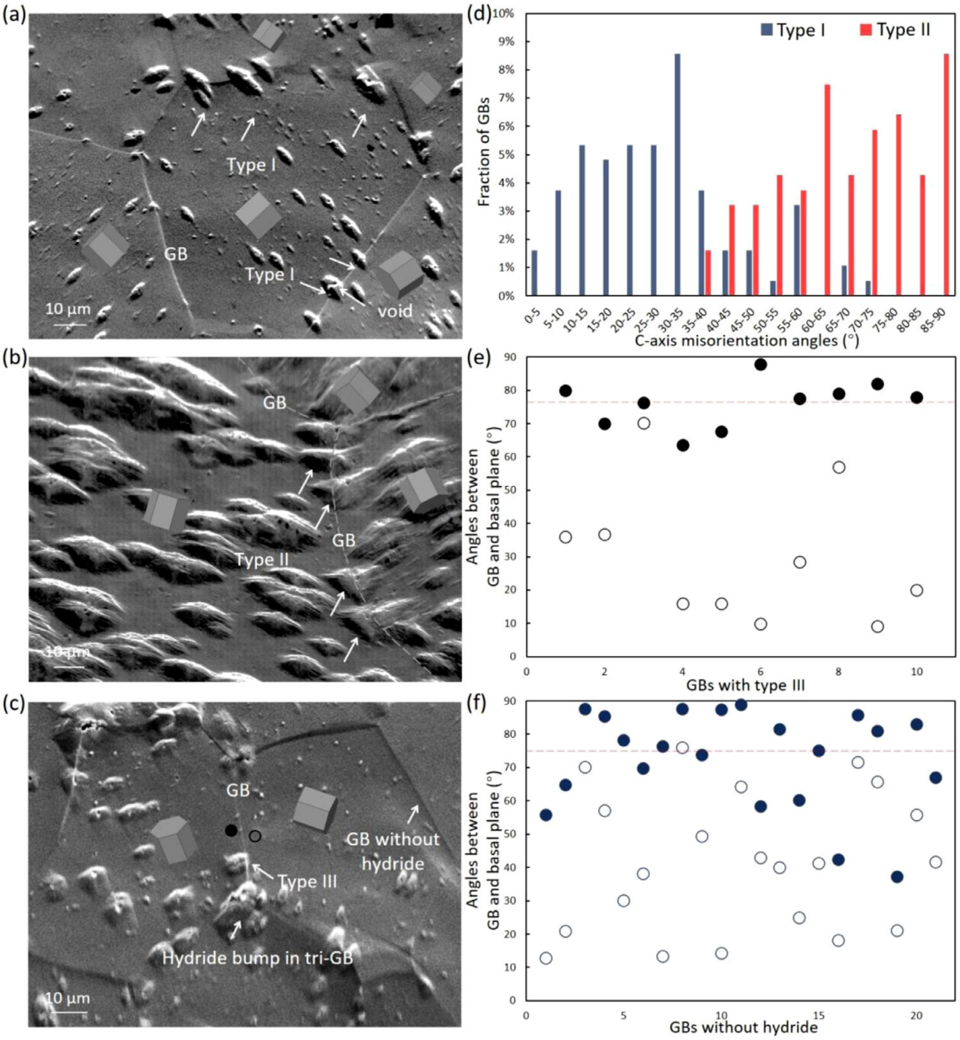

Fig. 12. (a) to (c) SEM images showing the three types of intergranular hydride bumps. (d) Distribution of type I and type II hydride bumps vs. c-axis misorientation. The statistics considered 187 GBs for charging time from 0.5 h to 48 h. For (e) and (f), the data of these GBs were from samples charging for 10 min, 0.5 h and 1 h. (e) Distribution of type III hydride bumps vs. GB plane-basal plane angle. The solid circle marks grains adjacent to hydrides and the open symbol indicates grains without hydrides. (f) Characteristics of GBs without hydrides. A high fraction of such GBs has one side of the grain with the basal plane perpendicular to the GB. The solid and open circles indicate the two grains adjacent to GBs.

5. Conclusions

In this work, the precipitation, morphology evolution, distribution of intragranular and intergranular subsurface hydrides under stress-free conditions are investigated. By increasing the hydrogen charging time, the hydride bump formation process can be investigated in two stages: nucleation (charging time <6 h) and coalescence (>6 h). From these studies, the following conclusions can be drawn.

1. The subsurface intragranular hydride morphology depends on the grain orientation. Two types of hydride bumps–circular-like and needle-like–are identified based on the interacting angle between the basal plane and sample surface.
2. The phase transition sequence of subsurface hydrides is γ-ZrH $\rightarrow$ δ-ZrH$_{1.66}$ $\rightarrow$ ε-ZrH$_2$. Two orientation relationships between α-Zr and these hydrides are identified: $(0001)_\alpha||(11\bar{1})_\delta$ and $[2\bar{1}\bar{1}0]_\alpha||[011]_\delta$, and $(0001)_\alpha||(001)_\gamma/_\delta$ and $[1\bar{2}10]_\alpha||[110]_\gamma/_\delta$. These results indicate that the γ hydride is also stable, and the γ-to-δ hydrides transformation occurs under continuous hydrogen charging.
3. Grain boundaries (GBs) with c-axis misorientations of $<15°$, $=55°$-$60°$ and $>85°$ are preferred subsurface hydride precipitation sites. Additionally, three types of intergranular hydrides are found. With c-axis misorientations less than 40°, the growth direction of the intergranular hydrides in two grains is maintained and type I hydride bumps form. Otherwise, type II intergranular hydride bumps are produced. The results can explain the formation mechanism of mesoscale hydrides in strongly textured Zr alloys.
4. The crystallographic orientation of the basal plane plays a vital role in the precipitation and distribution of both intragranular and intergranular hydrides. From the statistical analysis of GBs with only type III hydride or no hydride formation, it can be concluded that GBs with at least one neighbor grain basal plane perpendicular to the GB plane and with c-axis misorientation higher than 15° are resistant to hydride precipitation.

Declaration of Competing Interest

The authors declare no competing financial interests.

Acknowledgements

This research was supported by the National Natural Science Foundation of China (grant nos. 51922082, 51971170 and

51942104), the National Key Research and Development Program of China (2017YFB0702301), the 111 Project of China (grant number BP2018008) and the Innovation Project of Shaanxi Province (grant no. 2017KTPT-12).

References

[1] D.O. Northwood, U. Kosasih, Hydrides and delayed hydrogen cracking in zirconium and its alloys, Int. Mater. Rev. 28 (1983) 92–121.
[2] S. Yagnik, A. Garde, Zirconium alloys for LWR fuel cladding and core internals, in: G.R. Odette, S.J. Zinkle (Eds.), Structural Alloys for Nuclear Energy Applications, Elsevier, 2019, pp. 247–291.
[3] P. Rodriguez, Nuclear reactor materials: irradiation effects, in: K.H.J. Buschow, R.W. Cahn, M.C. Flemings, B. Ilschner, E.J. Kramer, S. Mahajan, P. Veyssière (Eds.), Encyclopedia of Materials: Science and Technology, Elsevier, 2001, pp. 6349–6361.
[4] R.A. Holt, In-reactor deformation of cold-worked Zr-2.5Nb pressure tubes, J. Nucl. Mater. 372 (2008) 182–214.
[5] G.J. Field, J.T. Dunn, B.A. Cheadle, Analysis of the pressure tube failure at pickering NGS “A” unit 2 nuclear systems department, Can. Metall. Q. 24 (1985) 181–188.
[6] , Interstitial ordering, in: S. Banerjee, P. Mukhopadhyay (Eds.), Phase Transformations Examples from Titanium and Zirconium Alloys, Elsevier, 2007, pp. 717–781.
[7] K. Une, S. Ishimoto, Dissolution and precipitation behavior of hydrides in Zircaloy-2 and high Fe Zircaloy, J. Nucl. Mater. 322 (2003) 66–72.
[8] R.N. Singh, S. Mukherjee, A. Gupta, S. Banerjee, Terminal solid solubility of hydrogen in Zr-alloy pressure tube materials, J. Alloy. Comp. 389 (2005) 102–112.
[9] J.J. Kearns, Terminal solubility and partitioning of hydrogen in the alpha phase of zirconium, Zircaloy-2 and Zircaloy-4, J. Nucl. Mater. 22 (1967) 292–303.
[10] R. Dutton, K. Nuttall, M.P. Puls, L.A. Simpson, Mechanisms of hydrogen induced delayed cracking in hydride forming materials, Metall. Trans. A 8 (1977) 1553–1562.
[11] L.A. Simpson, M.P. Puls, The effects of stress, temperature and hydrogen content on hydride-induced crack growth in Zr-2.5 pct Nb, Metall. Trans. A 10 (1979) 1093–1105.
[12] C.D. Cann, E.E. Sexton, An electron-optical study of hydride precipitation and growth at crack tips in zirconium, Acta Metall. 28 (1980) 1215–1221.
[13] Y.S. Kim, S.B. Ahn, Y.M. Cheong, Precipitation of crack tip hydrides in zirconium alloys, J. Alloy. Comp. 429 (2007) 221–226.
[14] R.N. Singh, R. Kishore, T.K. Sinha, B.P. Kashyap, Hydride blister formation in Zr-2.5wt%Nb pressure tube alloy, J. Nucl. Mater. 301 (2002) 153–164.
[15] G.J.C. Carpenter, J.F. Watters, R.W. Gilbert, Dislocation generated by zirconium hydride precipitates in zirconium and some of its alloys, J. Nucl. Mater. 48 (1973) 267–276.
[16] J.E. Bailey, Electron microscope observations on the precipitation of zirconium hydride in zirconium, Acta Metall. 11 (1963) 267–280.
[17] Y. Shinohara, H. Abe, T. Iwai, N. Sekimura, T. Kido, H. Yamamoto, T. Taguchi, In situ TEM observation of growth process of zirconium hydride in Zircaloy-4 during hydrogen ion implantation, J. Nucl. Sci. Technol. 46 (2009) 564–571.
[18] G.J.C. Carpenter, The precipitation of γ-zirconium hydride in zirconium, Acta Metall. 26 (1978) 1225–1235.
[19] W. Qin, N.A.P. Kiran Kumar, J.A. Szpunar, J. Kozinski, Intergranular δ-hydride nucleation and orientation in zirconium alloys, Acta Mater. 59 (2011) 7010–7021.
[20] N.A.P. Kiran Kumar, J.A. Szpunar, Z. He, Preferential precipitation of hydrides in textured zircaloy-4 sheets, J. Nucl. Mater. 403 (2010) 101–107.
[21] S.Y. Wang, F. Giuliani, T.B. Britton, Microstructure and formation mechanisms of δ-hydrides in variable grain size Zircaloy-4 studied by electron backscatter diffraction, Acta Mater. 169 (2019) 76–87.
[22] X.Q. Ma, S.Q. Shi, C.H. Woo, L.Q. Chen, Phase-field simulation of hydride precipitation in bi-crystalline zirconium, Scr. Mater. 47 (2002) 237–241.
[23] S. Yamanaka, K. Yoshioka, M. Uno, M. Katsura, H. Anada, T. Matsuda, S. Kobayashi, Thermal and mechanical properties of zirconium hydride, J. Alloy. Comp. 293-295 (1999) 23–29.
[24] L.A. Simpson, C.D. Cann, Fracture toughness of zirconium hydride and its influence on the crack resistance of zirconium alloys, J. Nucl. Mater. 87 (1979) 303–316.
[25] H.E. Weekes, V.A. Vorontsov, I.P. Dolbnya, J.D. Plummer, F. Giuliani, T.B. Britton, D. Dye, In situ micropillar deformation of hydrides in Zircaloy-4, Acta Mater. 92 (2015) 81–96.
[26] H.C. Chu, S.K. Wu, K.F. Chien, R.C. Kuo, Effect of radial hydrides on the axial and hoop mechanical properties of Zircaloy-4 cladding, J. Nucl. Mater. 362 (2007) 93–103.
[27] H. Chan, S.G. Roberts, J. Gong, Micro-scale fracture experiments on zirconium hydrides and phase boundaries, J. Nucl. Mater. 475 (2016) 105–112.
[28] Z. Zhao, J.P. Morniroli, A. Legris, A. Ambard, Y. Khin, L. Legras, M. Blat-Yrieix, Identification and characterization of a new zirconium hydride, J. Microsc. 232 (2008) 410–421.
[29] W. Zhu, R. Wang, G. Shu, P. Wu, H. Xiao, First-principles study of different polymorphs of crystalline zirconium hydride, J. Phys. Chem. C 114 (2010) 22361–22368.
[30] S.S. Sidhu, N.S Sataya-Murthy, F.P. Campos, D.D. Zauberis, Neutron and X-ray diffraction studies of nonstoichiometric metal hydrides, Adv. Chem. Ser. 39 (1963) 87–98.
[31] M.P. Cassidy, C.M. Wayman, The crystallography of hydride formation in zirconium: I. The $\delta \rightarrow \varepsilon$ transformation, Metall. Mater. Trans. A 11 (1980) 47–56.
[32] Q. Wang, S. Xu, J.S. Lecomte, C. Schuman, L. Peltier, X. Shen, W. Song, Crystallographic orientation dependence of hydride precipitation in commercial pure titanium, Acta Mater. 183 (2020) 329–339.
[33] T.W. Heo, K.B. Colas, A.T. Motta, L.Q. Chen, A phase-field model for hydride formation in polycrystalline metals: application to δ-hydride in zirconium alloys, Acta Mater. 181 (2019) 262–277.
[34] Y. Zhang, X.M. Bai, J. Yu, M.R. Tonks, M.J. Noordhoek, S.R. Phillpot, Homogeneous hydride formation path in α-Zr: molecular dynamics simulations with the charge-optimized many-body potential, Acta Mater. 111 (2016) 357–365.
[35] G.M. Han, Y.F. Zhao, C.B. Zhou, D.Y. Lin, X.Y. Zhu, J. Zhang, S.Y. Hu, H.F. Song, Phase-field modeling of stacking structure formation and transition of δ-hydride precipitates in zirconium, Acta Mater. 165 (2019) 528–546.
[36] G.J.C. Carpenter, The dilatational misfit of zirconium hydrides precipitated in zirconium, J. Nucl. Mater. 48 (1973) 264–266.
[37] C.D. Cann, M.P. Puls, E.E. Sexton, W.G. Hutchings, The effect of metallurgical factors on hydride phases in zirconium, J. Nucl. Mater. 126 (1984) 197–205.
[38] K.G. Barraclough, C.J. Beevers, The nature of the γ-phase in zirconium-hydrogen alloys, J. Less Common Met. 35 (1974) 177–180.
[39] J.S. Bradbrook, G.W. Lorimer, N. Ridley, The precipitation of zirconium hydride in zirconium and zircaloy-2, J. Nucl. Mater. 42 (1972) 142–160.
[40] G.C. Weatherly, The precipitation of γ-hydride plates in zirconium, Acta Metall. 29 (1981) 501–512.
[41] A.T.W. Barrow, A. Korinek, M.R. Daymond, Evaluating zirconium-zirconium hydride interfacial strains by nano-beam electron diffraction, J. Nucl. Mater. 432 (2013) 366–370.
[42] J. Bair, M.A. Zaeem, D. Schwen, Formation path of δ hydrides in zirconium by multiphase field modeling, Acta Mater. 123 (2017) 235–244.
[43] M.P. Cassidy, C.M. Wayman, The crystallography of hydride formation in zirconium: II. The $\delta \rightarrow \varepsilon$ transformation, Metall. Mater. Trans. A 11 (1980) 57–67.
[44] T. Maimaitiyili, A. Steuwer, J. Blomqvist, C. Bjerkén, M.S. Blackmur, O. Zanellato, J. Andrieux, F. Ribeiro, Observation of the δ to ε Zr-hydride transition by in-situ synchrotron X-ray diffraction, Cryst. Res. Technol. 51 (2016) 663–670.
[45] K.G. Barraclough, C.J. Beevers, Some observations on the phase transformations in zirconium hydrides, J. Nucl. Mater. 34 (1970) 125–134.
[46] B. Nath, G.W. Lorimer, N. Ridley, The relationship between gamma and delta hydrides in zirconium-hydrogen alloys of low hydrogen concentration, J. Nucl. Mater. 49 (1974) 262–280.
[47] E. Tulk, M. Kerr, M.R. Daymond, Study on the effects of matrix yield strength on hydride phase stability in Zircaloy-2 and Zr-2.5 wt% Nb, J. Nucl. Mater. 425 (2012) 93–104.
[48] W. Qin, J.A. Szpunar, J. Kozinski, Hydride-induced degradation of hoop ductility in textured zirconium-alloy tubes: a theoretical analysis, Acta Mater 60 (2012) 4845–4855.
[49] A. Banos, C.A. Stitt, T.B. Scott, The effect of sample preparation on uranium hydriding, Corros. Sci. 113 (2016) 91–103.
[50] R. Gremaud, M. Gonzalez-Silveira, Y. Pivak, S. de Man, M. Slaman, H. Schreuders, B. Dam, R. Griessen, Hydrogenography of PdHx thin films: influence of H-induced stress relaxation processes, Acta Mater. 57 (2009) 1209–1219.
[51] Y. Manassen, H. Realpe, Y. Greenbaum, N. Shamir, M.H. Mintz, R.Z. Shneck, Strain-dependent chemical reaction on inhomogeneous surfaces, J. Phys. Chem. C 120 (2016) 24197–24202.
[52] Z. Yang, P. Shi, B. Ao, Research progress on the desorption behavior of hydrides in zirconium alloys, Mater. Rep. 34 (2020) 05102–05108.
[53] T.B. Scott, G.C. Allen, I. Findlay, J. Glascott, UD$_3$ formation on uranium: evidence for grain boundary precipitation, Philos. Mag. 87 (2006) 177–187.
[54] R. Birch, S. Wang, V. Tong, B. Britton, The effect of cooling rate and grain size on hydride microstructure in Zircaloy-4, J. Nucl. Mater. 513 (2019) 221–225.
[55] B.B. He, B. Hu, H.W. Yen, G.J. Cheng, Z.K. Wang, H.W. Luo, M.X. Huang, High dislocation density-induced large ductility in deformed and partitioned steels, Science 357 (2017) 1029–1032.
[56] A. Akhtar, The nature of γ-hydride in crept zirconium single crystals, J. Nucl. Mater. 64 (1977) 86–92.
[57] F. Long, D. Kerr, G. Domizzi, Q. Wang, M.R. Daymond, Microstructure characterization of a hydride blister in Zircaloy-4 by EBSD and TEM, Acta Mater. 129 (2017) 450–461.
[58] M.P. Puls, S.Q. Shi, J. Rabier, Experimental studies of mechanical properties of solid zirconium hydrides, J. Nucl. Mater. 336 (2005) 73–80.
[59] S.C. Lumley, R.W. Grimes, S.T. Murphy, P.A. Burr, A. Chroneos, P.R. Chard–Tuckey, M.R. Wenman, The thermodynamics of hydride precipitation: the importance of entropy, enthalpy and disorder, Acta Mater. 79 (2014) 351–362.
[60] X. Zhu, D.Y. Lin, J. Fang, X.Y. Gao, Y.F. Zhao, H.F. Song, Structure and thermodynamic properties of zirconium hydrides by structure search method and first principles calculations, Comput. Mater. Sci. 150 (2018) 77–85.
[61] J Wang, I.J. Beyerlein, Atomic structures of symmetric tilt grain boundaries in hexagonal close packed (hcp) crystals, Model. Simul. Mat. Sci. Eng. 20 (2012) 0–22.
[62] J.F.R. Ambler, Grain boundary hydride in Zircaloy-2, J. Nucl. Mater. 28 (1968) 237–245.
[63] A.T. Motta, L. Capolungo, L.Q. Chen, M.N. Cinbiz, M.R. Daymond, D.A. Koss, E. Lacroix, G. Pastore, P.C.A. Simon, M.R. Tonks, B.D. Wirth, M.A. Zikry, Hydrogen in zirconium alloys: a review, J. Nucl. Mater. 518 (2019) 440–460.